Autonomous Field Measurements of CO_2 in the Atmospheric column with the Miniaturized Laser Heterodyne Radiometer (Mini-LHR)

H. R. Melroy,[1] E. L. Wilson,[2,*] G. B. Clarke,[1] L. E. Ott,[3] J. Mao,[4] A. K. Ramanathan,[4] M. L. McLinden[5]

[1]*American University, 4400 Massachusetts Avenue, Washington, DC, 20016, United States of America*
[2]*Laser Remote Sensing Laboratory, NASA Goddard Space Flight Center, 8800 Greenbelt Road, Greenbelt, Maryland, 20771, United States of America*
[3]*Global Modeling and Assimilation Office, NASA Goddard Space Flight Center, 8800 Greenbelt Road, Greenbelt, Maryland, 20771, United States of America*
[4]*Earth System Science Interdisciplinary Center, University of Maryland, College Park, MD 20740 United States of America*
[5]*Microwave Instrument and Technology Branch, NASA Goddard Space Flight Center, 8800 Greenbelt Road, Greenbelt, Maryland, 20771, United States of America*
*Corresponding author: Emily.L.Wilson@nasa.gov

We present column CO_2 measurements taken by the passive Miniaturized Laser Heterodyne Radiometer (Mini-LHR) at 1611.51 nm at the Mauna Loa Observatory (MLO) in Hawaii. The Mini-LHR was operated autonomously, during the month of May 2013 at this site, working in tandem with an AERONET sun photometer that measures aerosol optical depth at 15 minute intervals during daylight hours. Laser Heterodyne Radiometry has been used since the 1970s to measure atmospheric gases such as ozone, water vapor, methane, ammonia, chlorine monoxide, and nitrous oxide. This iteration of the technology utilizes distributed feedback lasers to produce a low-cost, small, portable sensor that has potential for global deployment. Applications of this instrument include supplementation of existing monitoring networks to provide denser global coverage, providing validation for larger satellite missions, and targeting regions of carbon flux uncertainty. Also presented here is a preliminary retrieval analysis and the performance analysis that demonstrates that the Mini-LHR responds extremely well to changes in the atmospheric absorption.

1. Introduction

Increasing atmospheric Carbon dioxide (CO_2) concentrations will exert a major influence on climate over the coming century. The rate of increase in atmospheric CO_2 depends critically on both the magnitude of anthropogenic emissions and the ability of natural land and ocean carbon reservoirs to absorb this emitted carbon. Over recent decades, approximately 40% of emitted anthropogenic CO_2 has remained in the atmosphere while the remainder has been stored in land and ocean sinks [1]. Despite advances in CO_2 modeling and observing capabilities, the processes governing the flux of carbon between the atmosphere, land, and oceans are not well understood, leading to considerable uncertainty in projections of future climate change.

Surface CO_2 measurements, made by a network of remote surface sites for several decades, have provided a strong constraint on the atmospheric CO_2 growth rate. However, due to their remote locations, they provide limited information on the spatial distribution of carbon sources and sinks. Precise column CO_2 measurements from satellites have been demonstrated to be useful for inferring fluxes [2-4], but the results can be strongly influenced by systematic errors contained in the data [5-7]. The ground-based TCCON has been critical in calibrating and validating satellite datasets from GOSAT and OCO-2 [2-4], and its independent utility for flux inference has also been demonstrated [8]. However, high instrument costs have limited the network size and currently less than 20 sites exist globally.

The Mini-LHR demonstrated in this work could contribute to the global effort to reduce flux uncertainties by further validating satellite observations and supplementing measurements of ground-based *in situ* [5] and column networks [4]. Existing networks are characterized by notable gaps such as South America and Africa, which limits understanding of carbon fluxes in these regions. Existing satellites are also unable to see through clouds, which limits observations in persistently cloudy regions. While the Mini-LHR's ability to observe is similarly limited by clouds, it can observe continuously throughout daylight hours, providing a greater opportunity to observe when breaks in clouds occur, or during times of the day when cloud obstruction is less frequent. The mini-LHR has been designed to operate in tandem with AERONET (an established global network of nearly 500 ground based instruments that measure aerosol optical depth [7]). This partnership provides a simplified path to global deployment into an established network. Tandem operation with AERONET may ultimately be beneficial for column CO_2 measurements, as it has been shown that aerosols can modulate regional carbon cycles. Here we present field measurements of CO_2 in the atmospheric column from the Mini-LHR operation at Mauna Loa Observatory, Hawaii.

2. The Mini-LHR Instrument Design

The Mini-LHR is a simplified and compact version of a laser heterodyne radiometer [9-15] that measures the mole fractions of trace gases in the atmospheric column by combining sunlight that has undergone absorption by the trace gas with infrared laser light at an adjacent wavelength to the absorption feature. The schematic in Figure 1 shows a Mini-LHR arrangement for monitoring two separate gases simultaneously. This can be easily scaled to add more gas measurements with lasers selected to match the wavelength of the absorption feature (line) of interest. The CO_2 line monitored here is centered at 1611.51 nm (6205.34 cm^{-1}) and is the P(26e) transition of the $(14^01) – (00^00)$ vibrational band centered at 1605.65 nm (6228 cm^{-1}).
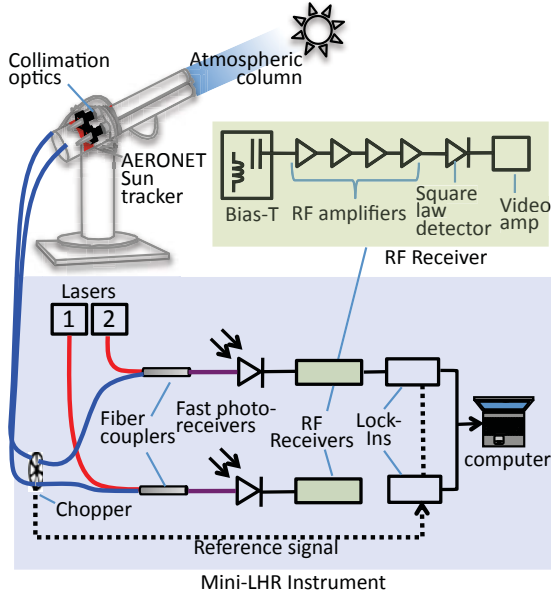

Fig. 1 Mini-LHR instrument schematic (shaded blue) operated in tandem with an AERONET sun tracker (upper left). Sunlight that has passed through CO_2 in the atmosphere is collected with collimation optics and then modulated with an optical chopper. The modulated sunlight is then superimposed with light from a DFB laser (laser 1) at 1611.5 nm in a single mode fiber coupler, and mixed in a fast photoreceiver (InGaAs detector). A custom RF receiver (shaded green) detects and amplifies the resulting beat signal which is collected with a lock-in amplifier as the laser scans through the CO_2 absorption feature. Components are also shown for a second channel that uses Laser 2 to measure an additional gas such as methane.

For each measurement, sunlight is collected with fiber-coupled collimation optics (~0.2 degree field of view) connected to an AERONET sun tracker (CIMEL Electronique model CE-318), which has a pointing accuracy of ~0.1 degrees [16]. Zenith and azimuth stepping motors point the tracker to the calculated position of the sun (based on GPS coordinates and time of day), then a four-quadrant detector updates the tracker's position every 30 seconds [17]. Collected sunlight passes through a single mode optical fiber (core diameter of 9.0 μm, 0.13 numerical aperture), is amplitude modulated with an optical chopper (at 200 Hz), and then superimposed with light from an extended L-band distributed feed-back laser at 1611.51 nm (local oscillator) in a single mode fiber coupler. Superimposed light is mixed in an InGaAs detector, producing an RF beat signal that is passed to the RF receiver.

Within the RF receiver, the beat signal passes through a bias-T (with a 50 ohm resistor) to separate the RF and DC outputs from the InGaAs detector. The RF output continues through a series of four amplifiers and is detected with a square law detector to produce an output voltage that is then further amplified and low-pass filtered with a video operational amplifier circuit (300 MHz bandwidth).

For each scan, the laser is step-scanned across the absorption feature and the signal from the RF receiver is measured with a lock-in amplifier that is referenced to the optical chopper. Each scan takes approximately one minute and consists of 55 points with a resolution of 0.002 nm over the feature and 0.01 nm across the wings, with an integration time of 500 ms for each point. Custom python software operated from a laptop computer controls the laser scanning and collects data from the lock-in amplifier.

$$E = E_L e^{i\omega_L} + E_S(\omega)e^{i\omega t}$$
$$\underbrace{\qquad}_{\text{Laserlight}} \underbrace{\qquad}_{\text{Sunlight}} \tag{1}$$

InGaAs detector
$$\left[\begin{aligned} I &\propto \left(E_L e^{i\omega_L t} + E_S(\omega)e^{i\omega t} \right) \cdot \left(E_L e^{-i\omega_L t} + E_S(\omega)e^{-i\omega t} \right) \\ &= E_L^2 + E_S^2 + 2E_L E_S \cos\left[(\omega_L - \omega)t \right] \end{aligned} \right. \tag{2}$$
$$\underbrace{\qquad}_{\text{DC}} \quad \underbrace{\qquad}_{\text{RF}}$$

Square law detector
$$\left[J(\omega) \propto I_{RF}^2 = 4E_L^2 E_S^2(\omega)\cos^2\left[(\omega_L - \omega)t \right] \right. \tag{3}$$

Lock-in amplifier
$$\left[N = \int J(\omega)f(\omega - \omega_L)d\omega = 2E_L^2 \int E_S^2(\omega)f(\omega - \omega_L)d\omega \right. \tag{4}$$

The data collected from the lock-in amplifier can be traced back to the solar irradiances at different wavelengths. Here in Eqns. 1 through 4, we trace the formation of the beat signal from the interference of sunlight with laser light. Eqn. 1 is the mixing
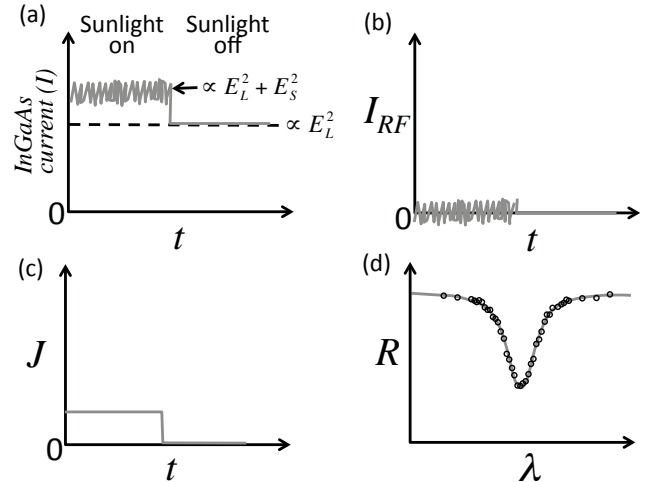

Fig. 2 Pictorial descriptions of the heterodyne process. The interference of sunlight and laser light on the InGaAs detector is shown in (a). The same signal after the DC component has been removed is shown in (b) where I_{RF} is the RF component of the InGaAs detector current. The output of the RF receiver is depicted in (c) where J (which has a frequency dependent response to sunlight) indicates the current output from the square law detector as a function of time. The integrated signal, or irradiance (R) is shown in (d) as the laser scans through the wavelengths of the absorption feature.

of laserlight and sunlight, where E is the combined electric field, E_L and E_S are the electric fields of laser and sunlight respectively, ω_L is the laser frequency, ω is the optical frequency of the sunlight that beats with the laser light and t is time as defined in an electric field. Eqn. 2 is the measurement of the current I, by the fast photoreceiver which is proportional to the light intensity with both DC and RF components indicated. Eqn. 3 shows the current output J, of the square law detector which is proportional to the square of the RF component of the fast photoreceiver. The resulting measurement of the RF receiver output is shown in Eqn. 4 as measured on the lock-in amplifier. The lock-in amplifier detects the demodulated signal referenced to the chopper frequency integrated over the instrument bandwidth. The output of the lock-in amplifier is proportional to the integrated solar irradiance within the instrument bandpass function f. An example of the implementation of this is shown with field data in Section 4.4. Figure 2 pictorially depicts the heterodyne process in these equations where Eqn. 2 corresponds to (a) and its RF component to (b). Eqn. 3 corresponds to (c) which is the output of the RF receiver, and Eqn 4 corresponds to (d) which is the result of an entire scan of CO_2.

3 Field Site Description

Data in this paper was taken at the Mauna Loa Observatory (MLO) in Hawaii (Coordinates: 19.5362°N 155.5763°W, Elevation: 3397masl) where Scripps Research Institute and NOAA have been monitoring *in-situ* carbon dioxide since the 1950's [18, 19]. This field site provided a unique high altitude platform to test performance of the Mini-LHR, autonomous operation (the Mini-LHR operated unattended for the entire month of the field campaign, May 2013), component lifetimes, and modes of tandem operation with the AERONET sun tracker. The data was then used to develop the data analysis software to be discussed in Section 5.

Fig. 3 The mini-LHR instrument is shown at the Mauna Loa Observatory in Hawaii. MLO is the site of the longest running measurements of atmospheric CO_2, begun in the late 1950s by Charles Keeling. MLO offers a unique testing environment for the mini-LHR, as the altitude helps ensure the atmosphere sampled represents the "background" signal of the atmosphere.

During the autonomous operation, the Mini-LHR was synchronized with the AERONET instrument operating in AUTO mode. In this configuration, data is collected within the ~2 minute AERONET observation window which occurs approximately every 15 minutes during daylight hours. Figure 3 shows the mini-LHR instrument operating in tandem with an AERONET sun tracker at MLO with Mauna Kea volcano visible in the background.

4 Radiative transfer simulations

The measurement simulation implements a high spectral resolution radiative transfer model to calculate the transmittance through a given optical path in the atmosphere. The Line-By-Line Radiative Transfer Model (LBLRTM) [20, 21] was used with the HIgh-resolution TRANsmission molecular absorption (HITRAN) database [22] as input. Voigt line profiles were used to simulate the absorption lineshape and line mixing [23] was added to the absorption calculations. Meteorological data such as atmospheric vertical profiles of pressure, temperature and water vapor, were taken from NASA's Modern Era Retrospective Analysis for Research and Applications (MERRA)[24] and interpolated to measurement sites and time as ancillary data for absorption calculations. Data are drawn from the 6-hr analyzed fields on the full model resolution and interpolated to measurement sites and time as ancillary data for atmospheric
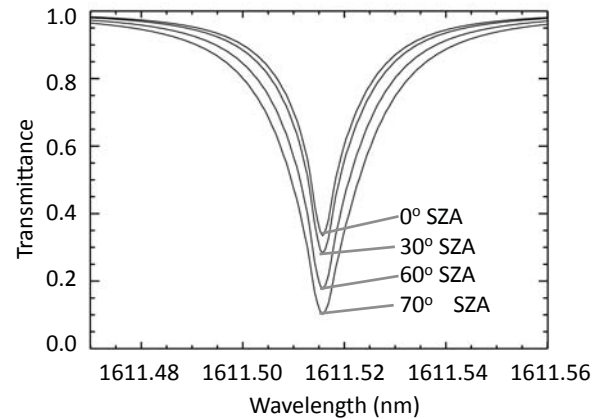

Fig. 4 Simulated total column transmittance for the measurement line centered at 1561.515 nm at Mauna Loa, Hawaii, at 18 Z (UTC) on May 4, 2013. Each curve corresponds to the solar zenith angle of 0, 30°, 60° and 70°, respectively and show decrease in transmittance as solar zenith angle increases.

absorption calculations. The top-of-the-atmosphere of the model data is around 76-km.

Both CO_2 and H_2O absorptions and Rayleigh extinction were included in the total absorption calculations and atmospheric refraction was also included, which can significantly change the light path length at large solar zenith angles.

Figure 4 illustrates the total column transmittance as a function of incident solar zenith angle at the top-of-the-atmosphere for the measurement line. Figure 4 shows the substantial effect of atmospheric refraction at a large solar zenith angle of 70°, which causes up to 0.35 in the optical depth at the Mauna Loa, Hawaii, or ranging 10-15% cross the whole line. The effect should be greater if the column extends down to sea level.
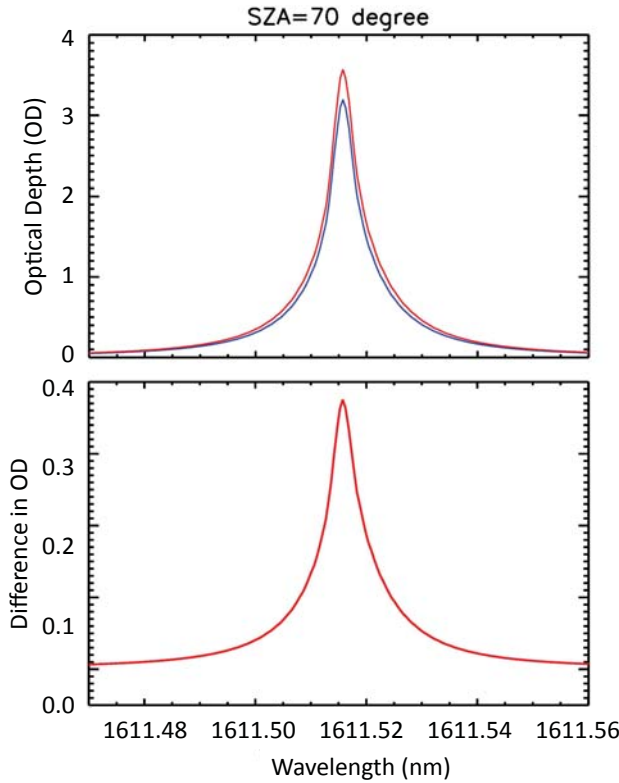
Fig. 5 At large solar zenith angles, the impact of atmospheric refraction is more significant. The top panel shows the modeled total column optical depth for the same line plotted in Figure 3 for an incident solar zenith angle of 70° at the top of the atmosphere, with atmospheric refraction (in red) and without (blue). The difference in these total column transmittances are shown in the bottom panel where a 10-15% difference in OD is equivalent to 40-50 ppm.

5 Data Handling and Analysis

Scans of CO_2 collected by the Mini-LHR include date, time, laser wavelength and lock-in signal. While data analysis is currently completed after the campaign, efforts are underway to incorporate data analysis into the acquisition software for real time measurements.

There are four steps to retrieving the CO_2 concentration. We first calculate the zenith transmittance for fixed atmospheric CO_2 using a radiative transfer model. Then we scale the absorption depending on the solar zenith angle at the time of measurement. Next, we convolve the scaled transmittance with the instrument lineshape to factor in instrument line broadening. Finally, we fit this broadened lineshape to the LHR data and retrieve the CO_2 concentration.

5.1 Scaling the absorption for the appropriate Solar Zenith Angle

The solar zenith angle was calculated based on the time of the day, the day of the year and the latitude and longitude [25]. The absorption was scaled by a factor of 1/cos(SZA), where SZA is the solar zenith angle. In addition, atmospheric refraction was also

factored in [26], which mainly had an effect for SZAs above 60 degrees.

5.2 Convolution with instrument lineshape

Prior to fitting the calculated transmittance lineshape with the data, we need to factor the instrument response, $f(\Delta\omega)$ where $\Delta\omega$ is the frequency difference between sunlight and laser light. The instrument response function of the Mini-LHR was characterized by mixing light from the scanning laser within the Mini-LHR instrument with light from a second, fixed laser (in lieu of sunlight) and recording the beat signal as a function of the scanning laser frequency as described in Clarke, et al. [27]. In this characterization, the first laser was scanned from 1611.38 – 1611.64 nm while the second laser was held constant at 1611.51 nm and the resulting instrument response bandwidth was 1.427 ± 0.005 GHz.

The calculated transmittance was convolved with the instrument response function, which broadened the lineshape. An example of this broadening on a calculated lineshape is shown in Figure 6.
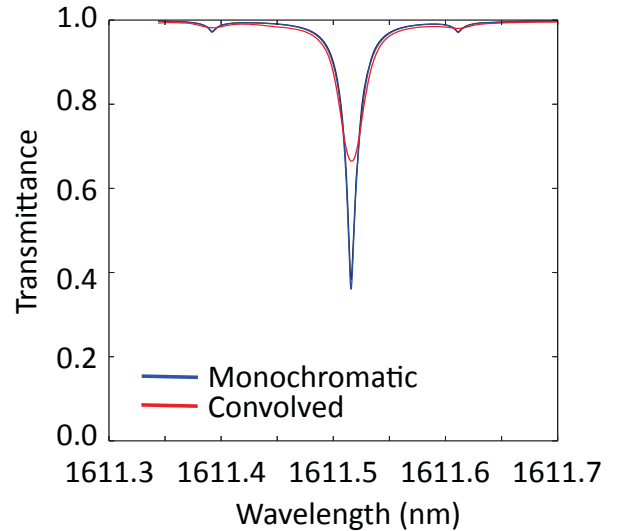

Fig. 6 Effect of instrument line broadening : The 1.5 GHz heterodyne bandwidth causes the lineshape to be broadened. For this reason, prior to fitting data to calculations, we convolve the calculated transmitted lineshape with the instrument response as shown in this plot.

5.3 Analysis of field data

The field data is read out of the lock-in amplifier in units proportional to the lock-in voltage signal. As shown earlier the final output is directly proportional to the sunlight within the instrument bandwidth of the reference laser frequency. To convert the field data to units of transmittance, we normalize the data by the mean signal of the off-line wavelengths (<1611.46 nm or >1611.57 nm). This measured transmittance is fitted to the calculations with two adjustable parameters – the wavelength offset and the CO_2 concentration. The CO_2 concentration parameter is a single scaling factor of the calculated transmittance, similar to Wunch, et al.[28].

For the field campaign at Mauna Loa Observatory, we applied an overall calibration scale factor of 1.22 to the absorption. This factor was based on calibrating data to *in-situ* MLO data on May 3, 2014. While the precise source of this scale factor is still being investigated, the factor did not vary during the duration of the field campaign. A sample fit of the calculated transmittance to a wavelength scan from the data is shown in Figure 7.

After fitting calculated lineshapes to individual wavelength scans, we then looked at a comparison of the calculated absorption based on atmospheric path length (assuming a uniform 400 ppm CO_2 atmosphere) and the measured absorption (based on fit to data) for the entire campaign data May 6-25. This is plotted in Figure 8 and shows an excellent correlation with R^2=0.99. This shows that the mini-LHR responds as expected to changes in the atmospheric absorption path length arising from the position of the sun.
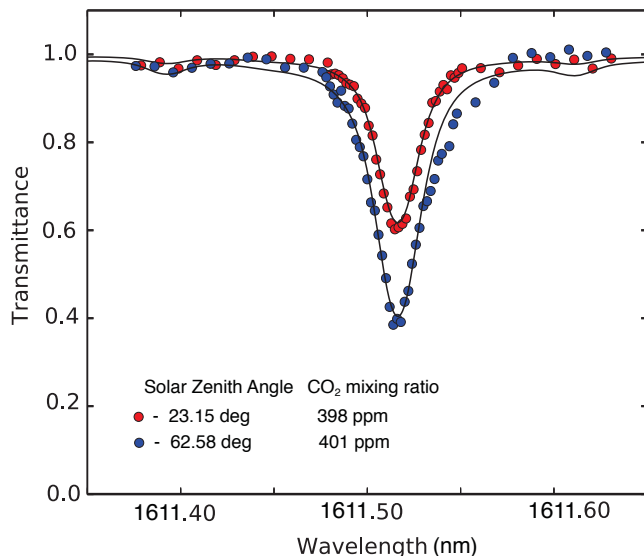

Fig. 8 Baseline instrument performance – The absorption measured by the LHR is compared against calculations based on the solar zenith angle (for fixed CO_2) for all cloud free data taken at MLO in May 2013. The high correlation coefficient shows that the change in absorption due to change in optical path length is completely captured by the LHR. This is a prerequisite for CO_2 concentration measurements. The absorptions are expressed in terms of the differential optical depth (DOD) between line center and off-line points.

retrieval and should be included in pathlength calculation for better fitting – especially for high solar zenith angles. Also, the retrieval algorithm currently uses a simple uniform vertical CO_2 profile. This could be improved by using a more sophisticated *a priori* vertical CO_2 profile that varies with time of year and location, similar to the approach of TCCON's retrieval [28]. Uncertainty in the atmospheric profiles (temperature, pressure, water vapor, and spectroscopic data base) can contribute to errors in the retrievals.

Fig. 7 Shown are representative transmittance spectra of the CO_2 absorption line centered at 1611.51 nm for single scans at two different solar zenith angles with the Mini-LHR at MLO. Experimental data (shown in circles) are fit with a simulated data (lines).

6. Discussion

Analysis of the field data has brought to light several necessary improvements to both the Mini-LHR instrument and the retrieval algorithm that will improve the sensitivity and reduce the instrument bias.

One improvement will be to implement a shorter scan time so that tens of scans can be made within the 2 minute AEROENT observation window. This will allow averaging of scans to reduce the random noise and improve measurement precision to the target of ~ 1 ppm. Data and analysis presented here has been of single, non-averaged scans which have a precision of ~6% due to the signal to noise ratio and duration of the scan. Other passive techniques such as TCCON also average multiple scans to reach their target precision.

The results here have demonstrated the capability of the instrument which has been shown to respond extremely well to changes in the atmospheric path length and therefore absorption. It was found that refraction made a significant difference in the
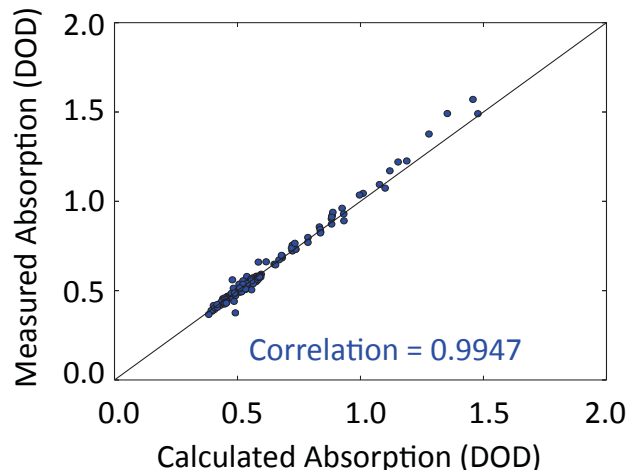
6. Conclusions

We have presented results from recent field testing at MLO as well as an analysis framework developed for data from the Mini-LHR instrument. Upcoming improvements will lower the instrument noise and yield CO_2 volume mixing ratio measurements in the ~ 1 ppm sensitivity range. Improvements will include a commercialized low-noise RF receiver that is currently under development, shorter scan times, multi-scan averaging. Future comparisons with TCCON and airborne *in-situ* measurements will inform additional improvements to the instrument and retrieval algorithm.

References

1. W. Knorr, "Is the airborne fraction of anthropogenic CO2 emissions increasing?," Geophys. Res. Lett **36**, doi:10.1002/2013GL059174 (2009).

2. S. Basu, M. Krol, A. Butz, C. Clerbaux, Y. Sawa, T. Machida, H. Matsueda, C. Frankenberg, O. P. Hasekamp, and I. Aben, " The seasonal variation of the CO2 flux over Tropical Asia estimated from GOSAT, CONTRAIL, and IASI," Geophys. Res. Lett. **41**, doi:10.1002/2013GL059105 (2014).

3. A. Chatterjee, R. J. Engelen, S. R. Kawa, C. Sweeney, and A. M. Michalak, "Background error covariance estimation for atmospheric CO2 data assimilation," J. Geophys. Res. Atmos. **118**, doi:10.1002/jgrd.50654 (2013).

4. S. Guerlet, S. Basu, A. Butz, M. Krol, P. Hahne, S. Houweling, O. P. Hasekamp, and I. Aben, "Reduced carbon uptake during the 2010 Northern Hemisphere summer from GOSAT," Geophys. Res. Lett **40**, doi:10.1002/grl.50402 (2013).

5. H. Takagi, et al., "Influence of differences in current GOSAT XCO2 retrievals on surface flux estimation," Geophys. Res. Lett **41**, doi:10.1002/2013GL059174 (2014).

6. F. Chevallier, P. I. Palmer, L. Feng, H. Boesch, C. W. O'Dell, and P. Bousquet, "Toward robust and consistent regional CO2 flux estimates from in situ and spaceborne measurements of atmospheric CO2," Geophys. Res. Lett **41**, doi:10.1002/2013GL058772 (2014).

7. S. Basu, et al., "Global CO2 fluxes estimated from GOSAT retrievals of total column CO2," Atmos. Chem. Phys. **13**, doi:10.5194/acp-5113-8695-2013 (2013).

8. F. Chevallier and e. al., "Global CO2 fluxes inferred from surface air-sample measurements and from TCCON retrievals of the CO2 total column," Geophys. Res. Lett **38**, doi:10.1029/2011GL049899 (2011).

9. R. T. Menzies and M. S. Shumate, "Usefulness of the infrared heterodyne radiometer in remote sensing of atmospheric pollutants," Joint Conference on Sensing of Environmental Pollutants, 1-4 (1971).

10. D. Weidmann, W. J. Reburn, and K. M. Smith, "Retrieval of atmospheric ozone profiles from an infrared quantum cascade laser heterodyne radiometer: results and analysis," Applied Optics **46**, 7162-7171 (2007).

11. A. Delahaigue, D. Courtois, C. Thiebeaux, S. Kalite, and B. Parvitte, "Atmospheric laser heterodyne detection," infrared Physics and Technology **37**, 7-12 (1996).

12. R. K. Seals Jr., "Analysis of Tunable Laser Heterodyne Radiometry: Remote Sensing of Atmospheric Gases," AIAA Journal **12**, 1118-1122 (1974).

13. V. Zeninari, B. Parvitte, D. Courtois, A. Delahaigue, and C. Thiebeaux, "An instrument for atmospheric detection of NH3 by laser heterodyne radiometry," J. Quant. Spectros. Radiat. Transfer **59**, 353-359 (1998).

14. R. T. Menzies, "A Re-Evaluation of Laser Heterodyne Radiometer ClO Measurements," Geophysical Research Letters **10**, 729-732 (1983).

15. R. T. Menzies, "Monitoring Atmospheric Pollutants With A Heterodyne Radiometer Transmitter-Receiver," United States Patent **Patent number 3,766,380**(1973).

16. AERONET, "Aerosol Robotic Network," http://aeronet.gsfc.nasa.gov/ (2011).

17. B. N. Holben, T. F. Eck, I. Slutsker, D. Tanre, J. P. Buis, A. Setzer, E. Vermote, J. A. Reagan, Y. J. Kaufman, T. Nakajima, F. Lavenue, I. Jankowiak, and A. Smirnov, "AERONET - A federated instrument network and data archive for aerosol characterization," Remote Sensing of Environment **66**, 1-16 (1998).

18. C. D. Keeling, R. B. Bacastow, A. E. Bainbridge, C. A. Ekdahl, P. R. Guenther, L. S. Waterman, and J. F. S. Chin, "Atmospheric carbon dioxide variations at Mauna Loa Observatory, Hawaii," Tellus **28**, 538-551 (1976).

19. K. W. Thoning, P. P. Tans, and W. D. Komhyr, "Atmospheric carbon dioxide at Mauna Loa Observatory: 2. Analysis of the NOAA GMCC data, 1974–1985," Journal of Geophysical Research: Atmospheres (1984–2012) **94**, 8549-8565 (1989).

20. S. A. Clough, M. J. Iacono, and J. Moncet, "Line-by-line calculations of atmospheric fluxes and cooling rates: Application to water vapor," J. Geophys. Res. Atmos. **97**, 15,761-715,785 (1992).

21. S. A. Clough and M. J. Iacono, "Line-by-line calculation of atmospheric fluxes and cooling rates 2. Application to carbon dioxide, methane, nitrous oxide and the halocarbons," J. Geophys. Res. Atmos. **100**, 16,519-516,535 (1995).

22. L. S. Rothman, I. E. Gordon, A. Barbe, D. C. Benner, P. F. Bernath, M. Birk, V. Boudon, L. R. Brown, A. Campargue, J.-P. Champion, K. Chance, L. H. Coudert, V. Dana, V. M. Devi, S. Fally, J. M. Flaud, R. R. Gamache, and A. Goldman, "The HITRAN 2008 molecular spectroscopic database," J. Quant. Spectrosc. Radiat. Transf. **110**, 533-572 (2009).

23. J. Lamouroux, H. Tran, A. L. Laraia, R. R. Gamache, L. S. Rothman, I. E. Gordon, and J.-M. Hartmann, "Updated database plus software for line-mixing in CO2 infrared spectra and their test using laboratory spectra in the 1.5–2.3 μm region," J. Quant. Spectros. Radiat. Transfer **111**, 2321-2331 (2010).

24. M. M. Rienecker, et al., "MERRA: NASA's Modern-Era Retrospective Analysis for Research and Applications," J. Climate **24**, 3624-3648 (2011).

25. J. H. Meeus, *Astronomical Algorithms* (Willmann-Bell, Inc., 1991).

26. V. Rozenbert and R. B. Rodman, *Twilight: A Study in Atmospheric Optics* (Plenum Press New York, 1996).

27. G. B. Clarke, E. L. Wilson, J. H. Miller, and H. R. Melroy, "Uncertainty analysis for the miniaturized

laser heterodyne radiometer (mini-LHR)," Measurement Science and Technology **25**, 055204-055209 (2014).

28.   D. Wunch, G. C. Toon, -. F. Blavier, L., R. A. Washenfelder, J. Notholt, B. Connor, D. W. T. Griffith, V. Sherlock, and P. O. Wennberg, "The total carbon column observing network (TCCON)," Philos T R Soc A **369**, 2087-2112 (2011).